buildings

MDPI

Article

Effects of Particle Shape and Packing Density on the Mechanical Performance of Recycled Aggregates for Construction Purposes

Xin Tan [1,2], Zhaohui Qiu [1], Xin Yin [1,*], Yuegang Hu [1], Xiaoming Liu [1,2] and Lei Zeng [3]

[1] College of Civil Engineering, Hunan University, Changsha 410012, China; xintan@hnu.edu.cn (X.T.); lxmcivil@hnu.edu.cn (X.L.)
[2] Key Laboratory of Building Safety and Energy Efficiency, Ministry of Education, Hunan University, Changsha 410012, China
[3] Guangzhou Highway Co., Ltd., Guangzhou 510623, China
* Correspondence: yinx@hnu.edu.cn

Abstract: This paper employs the discrete element method (DEM) to study the mechanical properties of artificial crushed stone. Different grain shapes and gradations are considered, and three types of 3D artificial stone models are generated based on the statistical conclusions in the relevant literature and the observed data. Concurrently, the 3D models of the artificial stones are divided into three groups by their shape parameters (elongation index and flatness index). Furthermore, three types of gradation with different Cu (coefficient of uniformity) and Cc (coefficient of curvature) are also considered. Then, several 3D triaxial compression tests are conducted with the numerical methods to determine the relationship between the grain shapes and their mechanical characteristics. The test results showed that there was a positive correlation between a particles' angularities and the maximum deviatoric stress in the triaxial compression tests when there were obvious distinctions between the particles. In addition, gradations had a conspicuous impact on the stiffness of the sample. The stress–strain curve possessed a larger slope when the coefficient of curvature was bigger. In terms of shear strength, the results in this paper align well with the traditional shear strength envelope which are convincing for the dependability of the methods used in this paper. The radial deformation capacity and volume strain of the specimen during the triaxial compression tests are also examined. It is believed that there were great differences in deformability between different samples. At the mesoscopic level, the change in coordination number is identified as the fundamental reason for the change in volume strain trend.

Keywords: discrete element method; mechanical behavior; artificial stone; grain shape; numerical analysis; triaxial compression tests

Citation: Tan, X.; Qiu, Z.; Yin, X.; Hu, Y.; Liu, X.; Zeng, L. Effects of Particle Shape and Packing Density on the Mechanical Performance of Recycled Aggregates for Construction Purposes. *Buildings* **2023**, *13*, 2153. https://doi.org/10.3390/buildings13092153

Academic Editor: Antonio Caggiano

Received: 25 July 2023
Revised: 19 August 2023
Accepted: 22 August 2023
Published: 24 August 2023

1. Introduction

The construction materials used today, such as cement, aluminum, and steel, all have extremely high carbon emissions and have tremendously deteriorated the environment [1]. Thus, the urgency of finding available, environmentally friendly construction materials has become unneglectable. Recently, the number of studies about the reuse of abandoned construction waste has increased rapidly [2–7]. Compared to other materials, artificially crushed stone is not only easy to acquire, but it also possesses adequate strength to meet requirements [8]. Consequently, this material has already been commonly used in contemporary constructions such as stone columns and base courses. Researchers also have shown a lot of interest in the mechanical behavior of artificially crushed stone in the last few years [9,10]. But the existing studies have not taken the particularity of the grain morphology of artificially crushed stone into consideration. Unlike natural gravel, the artificially crushed stone has not undergone weathering or deposition, so the angularities

and gradation of its grains will always be different to the former (Figure 1). In the meanwhile, plenty of studies confirm that particle shape will influence mechanical behavior significantly [11–14]. Therefore, discussions about the mechanical behavior of artificially crushed stone with different grain morphologies are necessary.

(a) Waste Concrete Crushing and recycled aggregate

(b) Use of manufactured aggregate for road construction

(c) Use of manufactured aggregate for dam construction

Figure 1. Application of manufactured stone aggregates in engineering.

For the purpose of discussing the relationship between grain morphologies and mechanical behavior, three steps are needed. First of all, the key concern is how to quantify the granular shape. During the last century, various methods and equations have been proposed to interpret the shape of grains [15–17]. Hakon Wadell [15] first proposed the degree of true sphericity (Ds) and the degree of roundness (Dr) to express the form of irregular particles. Other scholars, such as Krumbein [18] and Swanson [19], have also suggested various different definitions. Based on this, R.D. J. Zheng and Hryciw [20] compared a number of calculation methods and concluded that the aspect ratio sphericity proposed by Mitchell and Soga [21] was the most precise sphericity definition method. Second, data collection also is important. Due to the improvement of the imaging and computer technologies, there are many available and precise approaches to evaluate grain shapes [22,23]. For example, laser scanning technology, dynamic image analysis, and computed tomography, have all been used in prior studies. The final step is to conduct tests to study the influence of grain shapes on mechanical characteristics.

Many results have shown that the granular shape affects attainable density [24], internal friction angle [25], shear strength [26], and many other mechanical parameters [27]. And when compared to numerical simulation methods, the laboratory tests are always limited by the test facility and the standard test environment. While the traditional finite element method (FEM) still leaves much to be desired in simulating granular shape since it is unable to consider the rotation and interlocking of particles [28], the distinct element method (DEM) can overwhelmingly avoid this deficiency. Studies [29–35] have shown that the DEM has a high degree of consistency in simulating the mechanical properties

of irregular particles. The microscale has been explored in prior studies [36–39], and the connection between the microscale and macroscale has been somewhat clarified.

In this paper, the corresponding mechanical behaviors of the artificially crushed stone with different grain shapes and gradations are discussed using the DEM method. Three-dimensional digital models of irregular particles are generated, and their detailed shape parameters are based on the statistical conclusions in the relevant literature and the observed data. The obtained numerical models are divided into three groups based on their angularities. Then, several triaxial compression tests are conducted to study the differences in their mechanical properties and analyze the connection between microscopic behavior and macroscopic response. In this way, this paper can give a simple reference for the practical use of the artificially crushed stone.

2. DEM Models

This paper will use the elongation index (EI) and the flatness index (FI) as an estimate to describe the shape of gravel particles, expressed by the following formulas:

$$EI = W/L \quad (1)$$

$$FI = H/W \quad (2)$$

where L is the length of the particle, W is the width, and H is the height. It is obvious that regardless of EI or FI, their values will never exceed 0 and 1. The closer the value is to 1, the more similar the particle's shape will be to a sphere.

Feng [29] used laser scanning technology to observe the particle morphology of a significant amount of artificial crushed stone used for embankment construction. The results showed that more than 70% of the gravel particles' EIs and FIs were concentrated between 0.6 and 0.85, with only a small portion of particles falling outside this range. Essentially, there were no gravel particles with both indexes greater than 0.85 or less than 0.6. The general distribution law is shown in Figure 2. The particles in region A are defined as medium-angular particles, while the crushed stone aggregate in regions B and C are defined as low-angular particles and high-angular particles, respectively.

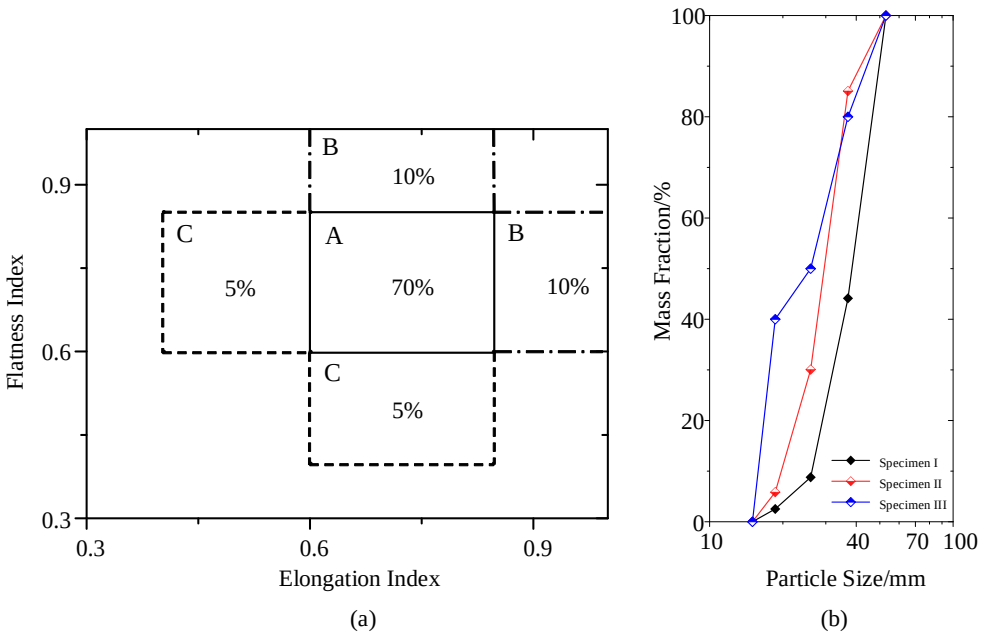

Figure 2. (**a**) Statistics of the morphology of the artificial crushed stone particles; (**b**) The grading curves of the stone aggregates used in the compression test.

Nine different templates are randomly generated for three different types of particles to reflect shape diversity, resulting in a total of 27 different models, as shown in Figure 3. It can be observed from the figure that there are significant differences in the morphology of the different types of particles.

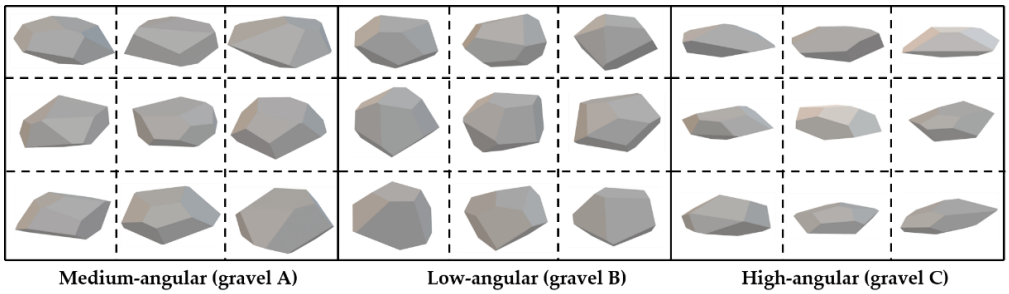

Figure 3. 3D models of the artificial crushed stone with different angularities.

The gradation of the crushed stone aggregate is represented by the three grading curves in Figure 2b. Curve I is derived from data measured in a laboratory triaxial test of crushed stone, while curves II and III are assumed from further discussion on the gradation. Detailed data for the gradation curves are provided in Tables 1 and 2.

Table 1. Detailed parameters of the grading curves.

Grading ID	d_{60}	d_{30}	d_{10}	C_u	C_c
I	31	26	19	1.63	1.15
II	41	32	26	1.58	0.96
III	29	17	15	1.93	0.66

C_u is the coefficient of uniformity; C_c is the coefficient of curvature.

Table 2. The initial elastic models of different tests.

Test ID	30 kPa	60 kPa	120 kPa	240 kPa
I	11.90	17.50	28.75	42.17
II	7.58	12.33	19.25	32.25
III	4.17	6.67	10.75	22.17
A	7.58	12.75	21.92	38.25
B	5.25	9.08	15.00	26.33
C	13.00	20.25	30.00	45.67

The numerical model and its profile for the triaxial compression test are shown in Figure 4. Since the crushed stone used in the research [40] is high-angular, the particle template used in this specimen is artificial crushed stone C, and the gradation follows curve II. The sample has a height of 600 mm, diameter of 300 mm, and a porosity of 45%. The intergranular contact model employed here is linear contact, where the contact stiffness (Ec) and the coefficient of friction (μ) are the most essential parameters.

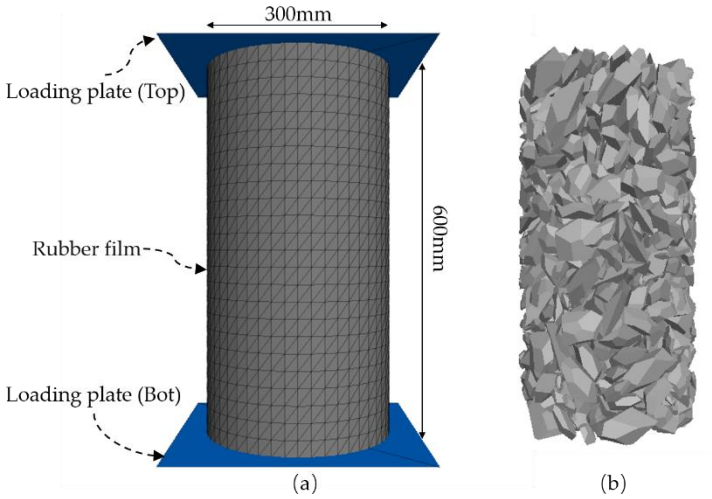

Figure 4. 3D numerical model of the triaxial compression specimen in PFC3D: (**a**) The loading plates and the side wall of the specimen; (**b**) The inside crushed stone aggregate.

In the triaxial compression test, the confining pressure was gradually increased from 1 kPa to 240 kPa, and the compression rate was controlled to generate 7% axial strain per minute (42 mm/min), achieved by assigning a constant speed to the rigid loading plates. The confining pressure was applied through shell nodes on the side wall, and the shell was generated by the coupling of FEM and DEM.

The stress–strain curve of the triaxial test can be seen in Figure 5. When comparing it to the result of the laboratory test, they are virtually the same when the confining pressure is 240 kPa. However, there is a certain degree of distinction in their deviatoric stress curves when the confining pressure is low. It is preliminarily believed that this phenomenon is caused by the breakage of high-angular crushed stone, which is not considered in the numerical simulation presented in this paper. This leads to the discrepancy in the stress–strain curves when particle breakage is prevalent in the specimen.

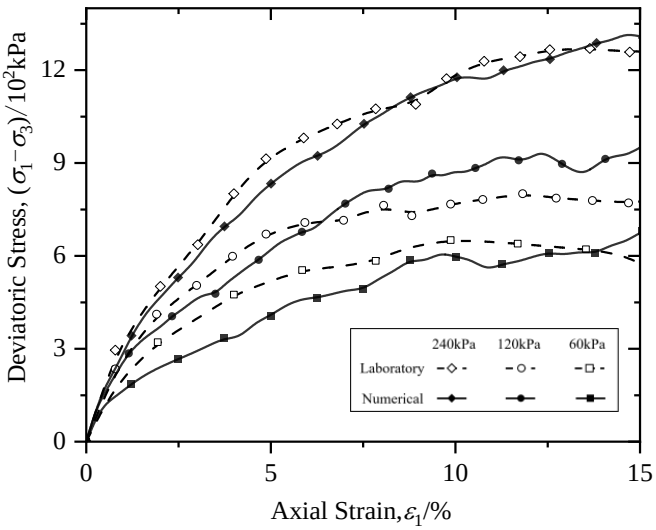

Figure 5. Comparison of the numerical results with the laboratory results.

Additionally, since the specific morphological parameters of the crushed stone used were not provided in the original literature, there may still be some differences between the real and numerical stone. However, it is undeniable that the DEM can accurately simulate the mechanical properties of the artificial crushed stone aggregate.

3. Mechanical Property

3.1. Stress–Strain Curve

In this section, additional specimens composed only of artificial crushed stone B (A) will be generated, as well as the sample (specimen N), which was made up of all three types of stone, as presented in Figure 1. Then, conventional triaxial compression tests are carried out on these four aggregates under different confining pressures, and the results can be seen in Figure 6. It is obvious that the higher the angularity, the larger the ultimate deviator stress of the specimen will be. Particularly for test C, its deviator stress corresponding to the axial strain reached 20%, which was significantly higher than that of the other three groups of samples. Furthermore, when the confining pressure was low, the results of test A and test B were very similar in the initial phase of the experiment. As the compression tests continued, specimen B entered the stress-softening period after reaching a peak value, while the deviatoric stress of test A began to fluctuate around a specific value. However, when it came to high confining pressure situations, the stiffness of test A and B showed a noticeable difference even when the axial strain was still negligible. Additionally, the stress-softening phenomenon of test B also became less pronounced.

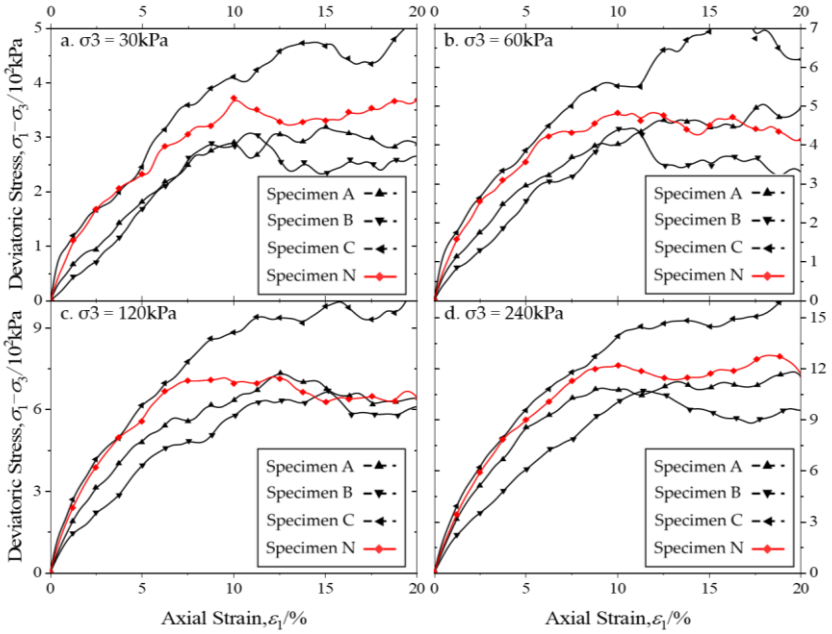

Figure 6. Typical stress–strain behavior during triaxial compression tests at different confining pressures on the crushed stone aggregate with different particles.

When the axial strain was below 7%, the stiffness of specimen N (the red curve in Figure 5) was almost the same as that of the high-angular artificial crushed stone aggregate. However, the slope of the stress–strain curve of test N appeared to decrease sharply after a critical point. The critical point occurred at different axial strain values depending on the confining pressure: approximately 5% for group A, 6% for group B, 7.5% for group C, and 9% for group D, while the confining pressure was 30 kPa. It is clear that the higher the confining pressure, the later the critical point appeared. Additionally, the final deviatoric stress of test N was similar to that of test A. In other words, the gravel components that determine the mechanical properties of the mixed artificial crushed stone aggregate will change at different compression stages. In the early stage, it is mainly controlled by the high-angular stone components, and in the later stage, it will be influenced by the medium-angular components.

To provide a clearer comparison of the similarities and discrepancies in these four tests, the deviatoric stress ratio ζ is proposed, which can be calculated by:

$$\varsigma = \frac{(\sigma 1 - \sigma 3)_A}{(\sigma 1 - \sigma 3)_N} \quad (3)$$

where the deviatoric stress of test N is taken as the standard value. If the value of ζ_A is 1, it means that the deviatoric stress of test A is equal to the result of test N at that moment. Due to space limitations, this paper only presents the deviatoric stress ratios under a confining pressure of 120 kPa (Figure 6).

From Figure 7, it can be observed that when the axial strain was between 3% and 6%, ζ_C was extremely close to 1, while the other two curves were both smaller than 1. After the axial strain reached 7%, the deviatoric stress ratios of all three groups started to increase until they reached 15%. The increasing trend of the three curves slowed down almost simultaneously. At this stage, the deviatoric stress ratio closest to 1 shifted to ζ_B.

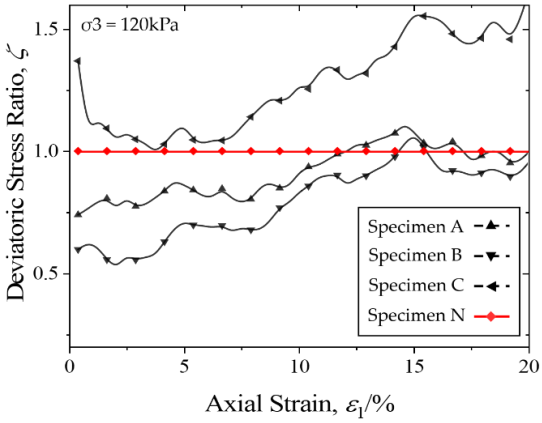

Figure 7. The deviatoric stress ratio of different specimens.

There is no significant disparity among the final deviatoric stresses of the gravel specimens with different gradations (Figure 8). However, it can be observed that the stiffness of specimen I is significantly greater than that of the other groups, and its deviatoric stress always reaches a stable value first. This suggests a positive correlation between the slope of the deviatoric stress and the coefficient of curvature of the crushed stone aggregate (C_c).

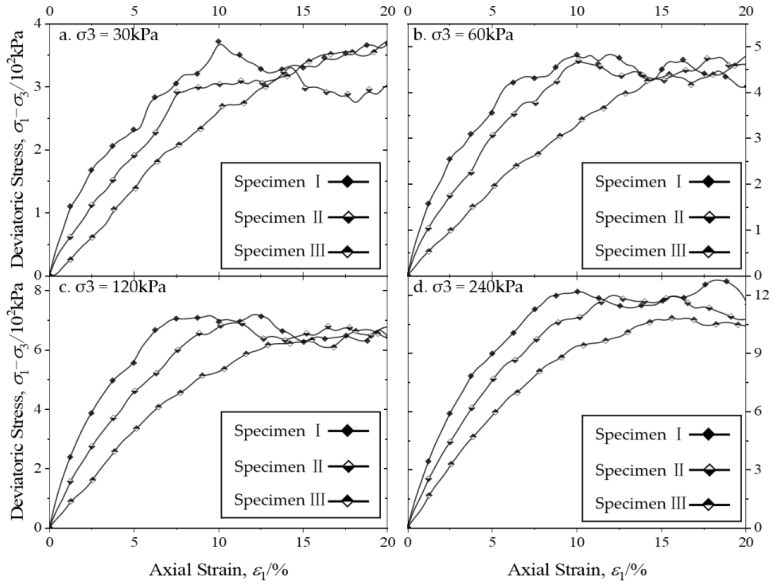

Figure 8. Typical stress–strain behavior during triaxial compression tests at different confining pressures on the crushed stone aggregate with different gradations.

Typically, the deviatoric stress curve of the crushed stone specimen can be approximated as a straight line when the axial strain is small, and its slope can be considered as the initial elastic modulus (E_i). Table 2 lists the initial elastic moduli of the specimens under different conditions. It is evident that both the growth of the C_c and the angularity enhance the Ei of the gravel aggregates. Moreover, as the confining pressure increases, the increment becomes more pronounced.

The Duncan-Chang constitutive relation proposes that the relationship between the initial elastic modulus of a soil sample (E_i) and the confining pressure (σ_3) in triaxial tests can be approximated as a linear logarithmic form. The mathematical expression for this relation is:

$$E_i = K \cdot p_a (\sigma_3 / p_a)^n \quad (4)$$

where K and n are dimensionless constants, and p_a represents standard atmospheric pressure, with a value of 101.4 kPa. Equation (4) remains applicable when considering the artificial crushed stone specimen (Figure 9). The detailed parameters of the fitting curve are listed in Table 3.

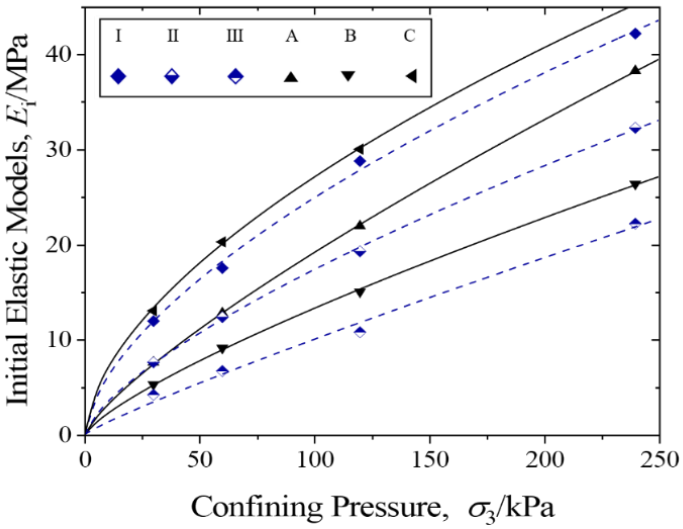

Figure 9. The relationship of the initial elastic models to the confining pressure of different specimens.

Table 3. The dimensionless constants of each fitting curve.

Parameters	I	II	III	A	B	C
K	247	172	100	190	132	269
n	0.61	0.70	0.89	0.79	0.78	0.59

From a microscopic perspective, the phenomenon can be explained by the interlocking capability of the crushed stone particles. Gravel with a larger size and higher angularity is typically more difficult to move within the aggregate. Additionally, the triaxial compression test inevitably involves the redistribution of the position of internal gravel particles and the disruption of their interlocking state. In other words, the deformation of a specimen composed of large-sized or high-angularity crushed stone particles requires more work from the loading plates. Consequently, when the axial strain remains constant, the corresponding deviatoric stress must be larger. From a macroscopic viewpoint, this results in an increase in the initial elastic models.

3.2. Shear Strength

For crushed stone aggregates, their shear strength envelopes generally follow the exponential function curves represented by the following normalized relationship:

$$\tau_f = A \cdot {\sigma_n}^b \quad (5)$$

where τ_f is the final shear strength, σ_n is the corresponding normal stress, and A and b are dimensionless constants. The envelope can be determined by several conventional Mohr circles under different stress conditions. The geometric representation is provided in Figure 9. The internal friction angle φ and the cohesion c both change with increasing confining pressure and can be described by the following formula:

$$c = A(1-b)\cdot{\sigma_n}^b \tag{6}$$

$$\varphi = \tan^{-1}\left(A\cdot b{\sigma_n}^{b-1}\right) \tag{7}$$

According to the geometric relationship in Figure 9, when the principal stresses of the gravel sample reach the limit state as σ_1 and σ_3, respectively, the corresponding normal stress of the failure surface should satisfy the following condition:

$$\sigma = \left(\frac{\sigma_1+\sigma_3}{2}\right) - \left(\frac{\sigma_1-\sigma_3}{2}\right)\cdot\sin\varphi \tag{8}$$

so that the values of φ and c can be calculated using the formula above.

Figure 10 shows the values of τ_f, φ, and c in a comparison diagram for different tests under a 240 kPa confining pressure. The increase in angularity significantly improves the shear strength of the aggregate. From the trend of the curve in Figure 10, it can be observed that the cohesion of the sample increases with the increase in normal stress. It is possible that the artificial crushed stone does not possess real cohesion, which is instead provided by the interlocking effect between adjacent particles, also known as "false cohesion". The increased normal stress undoubtedly leads to a closer relationship between the gravel particles in the sample, thus enhancing the cohesion. Similarly, specimen C also exhibits higher cohesion due to its stronger interlocking properties.

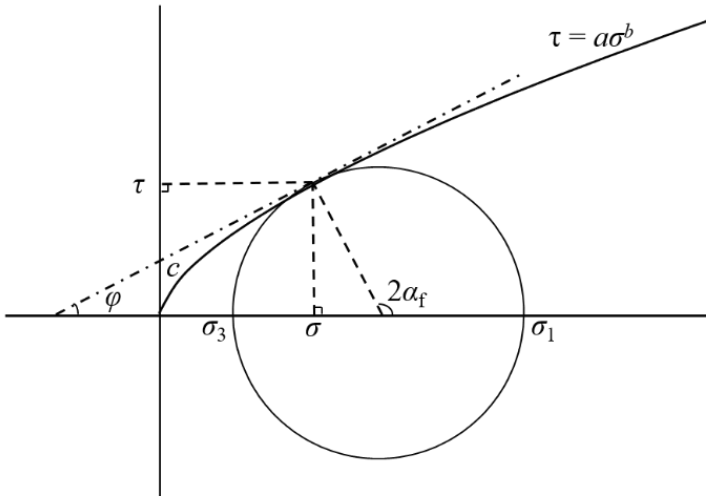

Figure 10. Geometric analysis of the shear strength envelope of crushed stone aggregates.

The internal friction angle of the crushed stone aggregate can be divided into three components:

1. The surface friction coefficient, φ_μ;
2. The additional work needed due to the deformation of the specimen, φ_v;
3. The rearrangement and fragmentation of gravel particles, φ_b.

It can be expressed by the following formula:

$$\varphi = \varphi_\mu + \varphi_v + \varphi_b \tag{9}$$

With an increase in normal stress, the expansion of the radial strain decreases, resulting in simpler rearrangement and a subsequent decrease in the internal friction angle. When the

shape of the gravel particles is closer to a sphere, less energy is required for internal transfer, leading to a relatively smaller internal friction angle.

Figure 11 displays a displacement profile cloud diagram in the z-direction for when the specimens reached the failure state under a 240 kPa confining pressure. The horizontal inclination angle of the shear plane of the three samples follows the order B < A < C, and the maturity of the shear band also increases with the increase in angularity. According to the Mohr–Coulomb strength theory, the relationship between the angle of internal friction and the inclination angle of the sample shear plane α_f should satisfy the following equation:

$$\alpha_f = \frac{\pi}{4} + \frac{\varphi}{2} \tag{10}$$

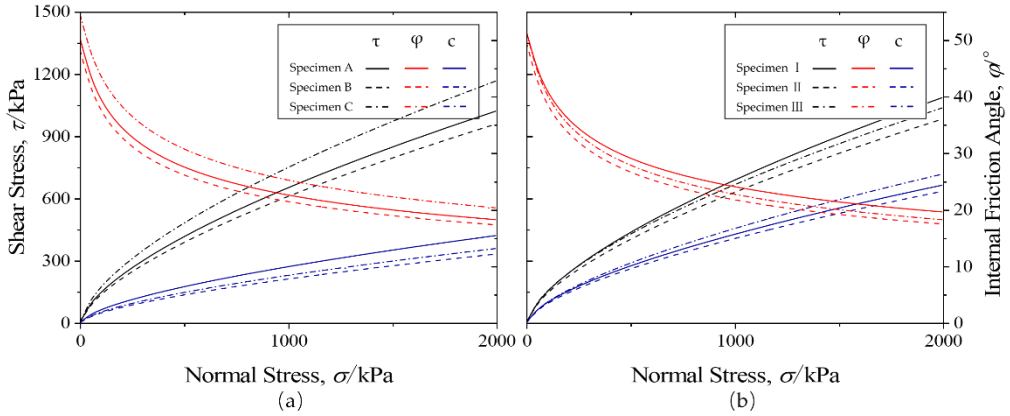

Figure 11. The shear strength and other mechanical properties of different crushed stone specimens: (**a**) different particle shapes; (**b**) different gradations.

As shown in Figure 12, the theoretical internal friction angles of the three groups of specimens under a 240 kPa confining pressure were 28.54°, 27.48°, and 29.78°, respectively. Consequently, the corresponding inclination angles of the failure surface were 59.27°, 58.74°, and 59.89°. Although the exact values may differ from those of the tests, the overall trend of change remains consistent.

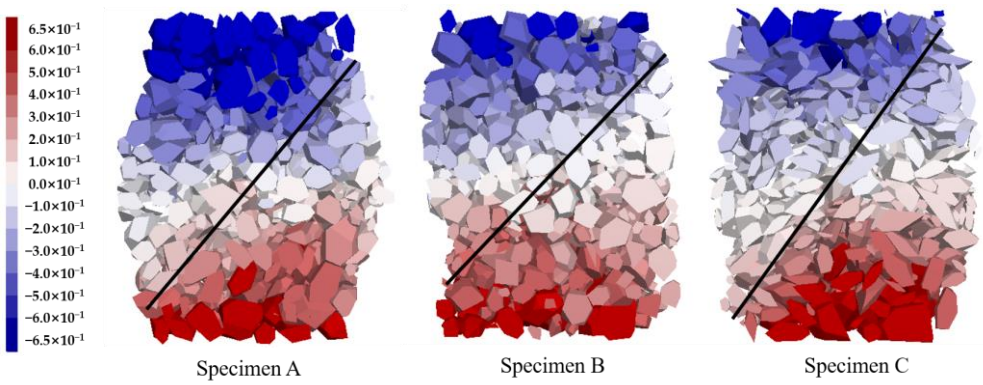

Figure 12. The displacement in z-direction of the internal particles in different specimens after shear failure.

4. Deformation Property

4.1. Poisson Ratio

The curves illustrating the variation of the radial strain with the axial strain for crushed stone samples with different particle configurations under a 240 kPa confining pressure demonstrate that specimen C consistently exhibits the greatest radial deflection (Figure 13). This indicates that the radial deformation capability of the crushed stone sample is enhanced with increasing angularity. However, the results for group A and group B are opposite: the

radial strain of specimen B, composed of stone particles closer to spheres, is larger than that of group A. By comparing the secant Poisson's ratio υ_s between different samples, it can be observed that as the tests progress, the secant Poisson's ratio corresponding to the sample steadily increases from the beginning to the end, but its rate of increase gradually slows down. Therefore, we can assume that the quantitative relationship between the secant Poisson's ratio and the axial strain of the gravel sample may follow a hyperbolic form.

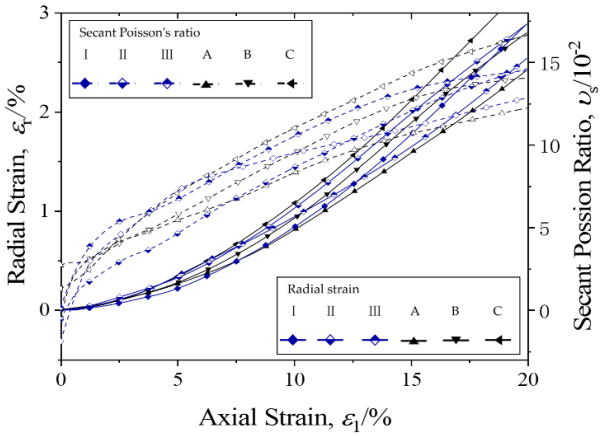

Figure 13. Variation of radial strain and the secant Poisson's ratio during the compression.

Figure 13 also presents a comparison of curves between different gradations of gravel samples. Compared to the impact caused by particle shape, the change in the radial deformation ability of samples due to gradation is not as significant. In different periods of the compression tests, the groups exhibiting the largest radial strain differ, and there are several intersections among the three curves.

Figure 14 displays the corresponding particle displacement profile nephograms in the x-direction under a 240 kPa confining pressure. For sample B and sample C, there is no apparent maximum displacement point in the middle of either specimen, and the shape of the lateral expansion line resembles a parabola. However, the upper and lower ends of sample A remain almost unchanged. This may be one of the reasons why the radial displacement ε_r of sample A is the smallest among the three groups. Among the three groups with different gradations, samples I and III, which have varying amounts of different-sized particles, demonstrate that the smaller particles effectively fill the pores between the larger particles, thereby improving the sample's resistance to deformation.

Considering that different pressures directly affect the transverse deformation performance of materials, the stress ratio σ_1/σ_3 and the corresponding tangential Poisson's ratio υ_t between groups A, B, and C under a 240 kPa confining pressure are compared in Figure 15. It is evident that the trends of these two ratios are quite similar, and the change in the secant Poisson's ratio lags behind the principal stress ratio to some extent, indicating a potential causal relationship between the two. In the case of test B, the principal stress ratio reaches a peak when the axial strain reaches approximately 10%, and the corresponding secant Poisson's ratio also peaks at an axial strain of about 15%. Similar corresponding results are observed in the test results of each group, suggesting that the variation in transverse deformation ability among different crushed stone aggregates is based on their shear properties.

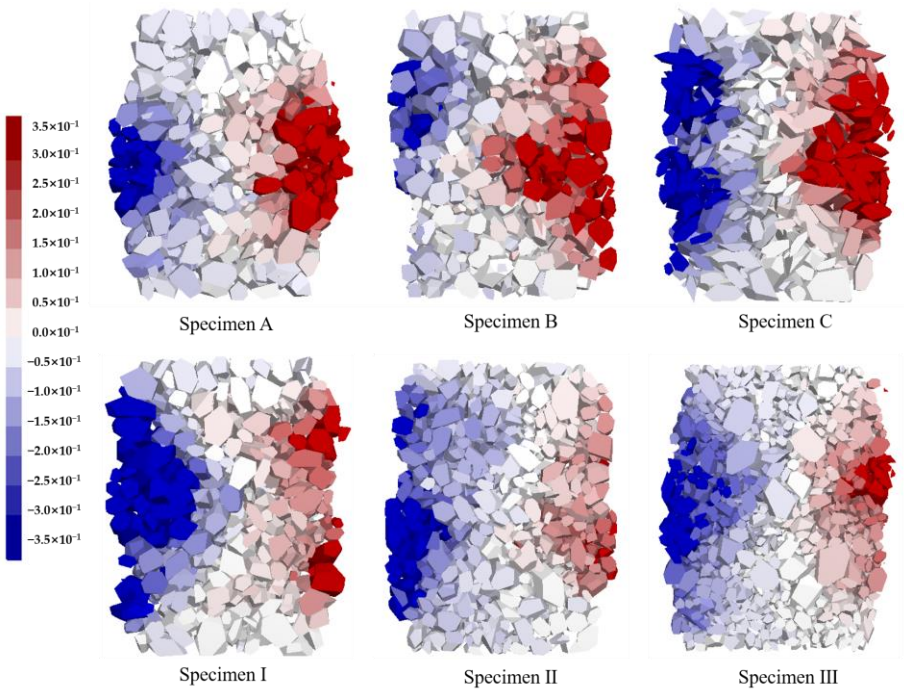

Figure 14. The displacement in x-direction of the internal particles in different specimens after shear failure.

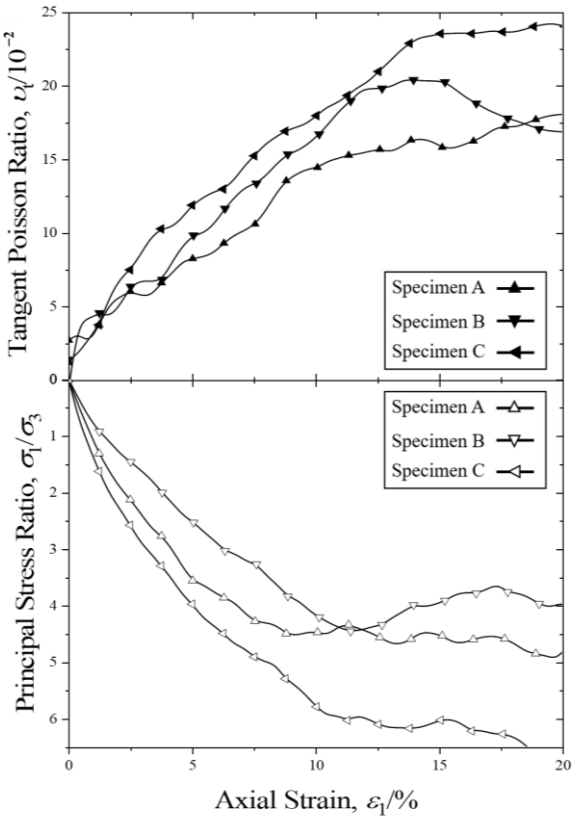

Figure 15. Comparison between the principal stress ratio and the tangent Poisson's ratio.

4.2. Volume Strain

As shown in Figure 16, the bulk strain variation of different groups under a 240 kPa confining pressure aligns with the common dilatancy model law of gravel aggregate, exhibiting a pattern of initial shrinkage followed by expansion. Analyzing the curves of

tests A, B, and C, it is evident that the dilatancy of group B surpasses that of groups A and C. This suggests that as the particle shape approaches a sphere, the crushed stone aggregates exhibit stronger dilatancy. Notably, the slope of the volume strain curve in test B is greater than that of the other two curves, while there appears to be no significant difference in dilatancy angle between specimens A and C. This observation may be attributed to the fact that gravel particles with low angularity have greater mobility, enabling easier slipping and rotation between adjacent particles under pressure. On the other hand, the interlocking force between high angular particles inhibits shear expansion. However, if the angularity is excessively high, the contact area and number of contacts between the particles decrease. Consequently, the mutual extrusion pressure among adjacent particles significantly increases, leading to an enhancement in dilatancy, as seen in samples A and C. Therefore, it can be inferred that there exists an optimal angularity for crushed stone to minimize volume strain in compression tests.

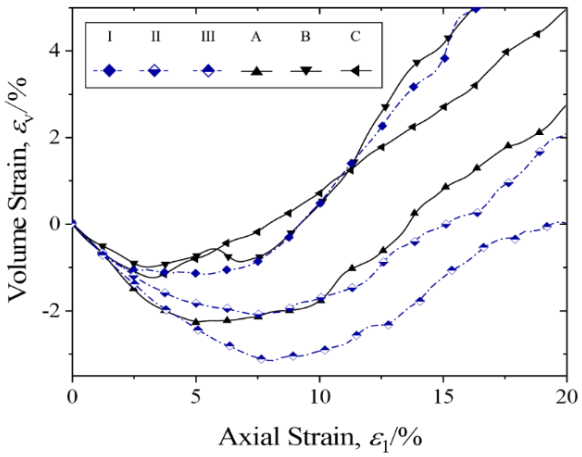

Figure 16. The variation of the volume strain in different triaxial compression tests.

Figure 16 displays the minimum volume strain ε_{vmin}, the axial strain ε1r corresponding to the restoration of the original volume, and the initial shear dilatancy angle ψ_i of different tests. It is evident that these parameters are generally positively correlated with angularity, irrespective of whether they are measured under low or high confining pressure.

With a decrease in the curvature coefficient, the corresponding aggregates exhibit a decline in their dilatancy. This can be attributed to the fact that gravel aggregates containing smaller particles can effectively fill the pores generated during the deformation process, thereby reducing porosity and resulting in a smaller shear dilatancy.

Throughout the analysis conducted above, a clear correlation between the dilatancy of crushed stone aggregates and their internal mesoscopic parameters can be observed. Consequently, contrast curves depicting the relationship between the dilatancy angle (ψ), coordination number (CN), and porosity (n) of different specimens under 240 kPa confining pressure are presented in Figure 14. These curves effectively illustrate the interrelationship among the three parameters. Initially, the porosity of each test experiences a slight decrease, followed by an increasing slope that gradually levels off after reaching the minimum value. The coordination number exhibits a rapid increase followed by a slow decrease. Concurrently, the dilatancy angle continuously increases from -30° to a positive value. The critical points associated with each parameter indicate that the coordination number reaches its peak first, while the dilatancy angle reaches its peak last. Consequently, it can be concluded that the alteration in the number of contacts within the specimen is the primary determinant of its overall expansion characteristics. Theoretically, there should exist a quantitative relationship between the volume strain of the sample and its internal contact state, thereby explaining how particle shape and aggregate gradation influence dilatancy.

In order to examine the changes in the contact within the crushed stone sample during compression, the fabric changes of test II under 240 kPa confining pressure are extracted

and presented in Figure 17. In Figure 18, it can be observed that the peak coordination number of this sample occurs at approximately 2–3% of the axial strain, as reflected in the fabric. Once the axial strain reaches 3%, the internal texture of the sample no longer undergoes significant changes. This indicates that the alterations in contact states within the 0–3% axial strain range are in response to the volume reduction of this specimen.

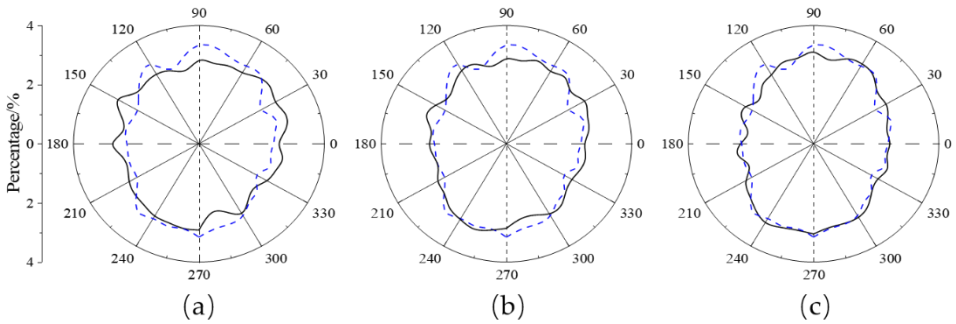

Figure 17. The variation of the fabric of the specimen during the tests: (**a**) 0% axial strain; (**b**) 1% axial strain; (**c**) 3% axial strain. (The blue dotted line is the fabric when the axial strain was 15%).

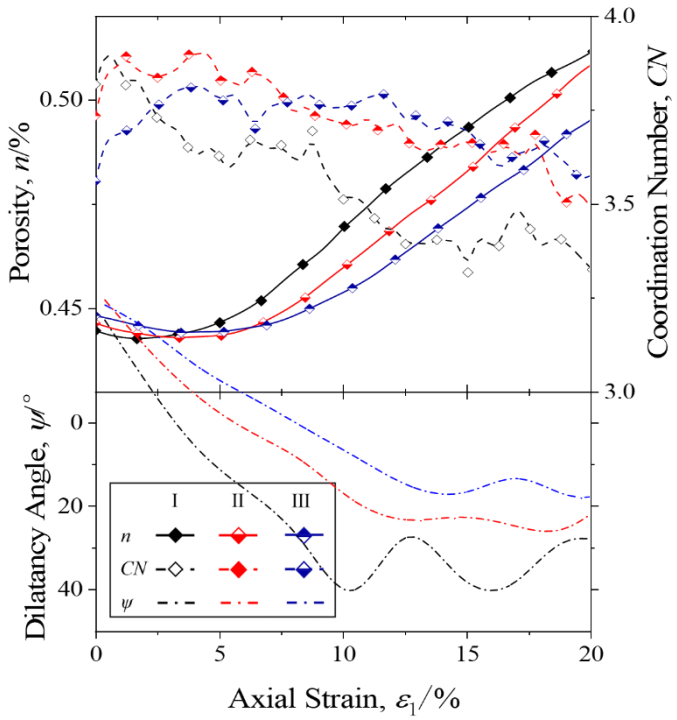

Figure 18. Comparison between different mesoscopic parameters of the artificial crushed stone specimens during the tests.

5. Conclusions

The results herein have proved that the methods used in this paper were credible reflections of the mechanical behavior of the irregular particles in triaxial tests. And the differences in angularities and gradations will obviously change the mechanical and deformation properties of the samples, which are revealed in:

1. The maximum deviatoric stress and the shear strength of the samples with higher angularities were significantly larger than those with medium and low angularities, while the final deviatoric stresses of samples with different gradations were nearly the same. Meanwhile, the initial elastic modulus increased when the curvature coefficient of the gradation curves became larger.

2. The variation patterns of pseudo-cohesion and the internal friction angle with the perimeter pressure for either group of samples were in accordance with the power function relationship proposed in earlier studies. At the same time, these two mechanical indexes also changed with the transformation of grain shape and gradation. The internal friction angle and cohesion increased with the enhancement of angularities and the curvature coefficient.
3. Clearly, all samples here showed a deformation trend with the greatest displacement seen in the middle, and the damage surface a diagonal line running through the specimen. However, it is obvious that the lateral deformation and the maturity of the damage surface are different between different groups of samples. Furthermore, it can be found from the axial strain and volume strain curves of different samples that the ones with higher angularities and higher curvature coefficients possess a better deformation capacity.
4. The changes of porosity (n), coordination number (CN), and shear expansion angle (ψ) during the compression tests were compared. It was found that the coordination number is the most sensitive microscopic index, which usually reached the maximum value and started to decrease when the axial strain was about 2–3%. On the contrary, in the other two cases, the axial strain corresponding to the extreme value was often greatly delayed. Therefore, it can be conjectured that the contact force and the number of particles was the fundamental reason for the difference in the mechanical behavior of different samples. This is also proven by the fabric changes of the samples.

This study utilizes a DEM gravel particle model, which overlooks particle fragmentation and may not fully account for surface roughness variations or potential concave polyhedral shapes. It examines the effects of particle shape on aggregate mechanical properties, considering both macroscopic and microscopic perspectives. However, it does not investigate aggregates mixed with different gravel angularities. Further exploration of the influence of other materials, such as fibers or concrete aggregates, and the conducting of more comprehensive macro–micro contact research, are potential areas for future study.

Author Contributions: Conceptualization, X.T. and L.Z.; methodology, Z.Q. and X.Y.; Numerical simulation, Z.Q., X.Y., Y.H. and X.L.; writing—original draft preparation, Z.Q.; writing—review and editing, X.T. and X.L. All authors have read and agreed to the published version of the manuscript.

Funding: This research was funded by the "National Natural Science Foundation of China (52278348)".

Data Availability Statement: Not applicable.

Conflicts of Interest: The authors declare no conflict of interest.

References

1. Bribián, I.Z.; Usón, A.A.; Scarpellini, S. Life cycle assessment in buildings: State-of-the-art and simplified LCA methodology as a complement for building certification. *Build. Environ.* **2009**, *44*, 2510–2520. [CrossRef]
2. Shaban, W.M.; Elbaz, K.; Amin, M.; Ashour, A. A new systematic firefly algorithm for forecasting the durability of reinforced recycled aggregate concrete. *Front. Struct. Civ. Eng.* **2022**, *16*, 329–346. [CrossRef]
3. Amin, M.; Hakeem, I.Y.; Zeyad, A.M. Influence of recycled aggregates and carbon nanofibres on properties of ultra-high-performance concrete under elevated temperatures. *Case Stud. Constr. Mater.* **2022**, *16*, e01063. [CrossRef]
4. Younis, M.; Amin, M.; Tahwia, A.M. Durability and mechanical characteristics of sustainable self-curing concrete utilizing crushed ceramic and brick wastes. *Case Stud. Constr. Mater.* **2022**, *17*, e01251. [CrossRef]
5. Hakeem, I.Y.; Alharthai, M.; Amin, M.; Zeyad, A.M.; Tayeh, B.A.; Agwa, I.S. Properties of sustainable high-strength concrete containing large quantities of industrial wastes, nanosilica and recycled aggregates. *J. Mater. Res. Technol.* **2023**, *24*, 7444–7461. [CrossRef]
6. Srikanth, K.S.; Lalitha, G. Mechanical performance of sustainable ternary blended self compacting concrete with waste crushed glass. *Mater. Today Proc.* **2022**, *60*, 394–398. [CrossRef]
7. Başaran, B.; Aksoylu, C.; Özkılıç, Y.O.; Karalar, M.; Hakamy, A. Shear behaviour of reinforced concrete beams utilizing waste marble powder. *Structures* **2023**, *54*, 1090–1100. [CrossRef]
8. Lan, W.W.; Zhong, R.F.; Lv, B.; Gan, J.Y.; Ying, J.W. Compressive strength of artificial sand recycled concrete with different content of stone powder. *Appl. Mech. Mater.* **2014**, *578–579*, 464–468. [CrossRef]
9. Lee, M.G.; Lo, S.L.; Kan, Y.C.; Chiang, C.H.; Chang, J.H.; Yu-Min, S.; Yatsenko, E.A.; Hu, S.-H. Water quenched slag from incinerator ash used as artificial stone. *Case Stud. Constr. Mater.* **2022**, *16*, e00827. [CrossRef]

10. Dongyu, C.; Meizhu, C.; Yuanhang, S.; Shaopeng, W.; Xintao, Z.; Chen, W. Sustainable use of recycled cement concrete with gradation carbonation in artificial stone: Preparation and characterization. *Constr. Build. Mater.* **2023**, *364*, 129867. [CrossRef]
11. Ting, J.M.; Meachum, L.; Rowell, J.D. Effect of particle shape on the strength and deformation mechanisms of ellipse-shaped granular assemblages. *Eng. Comput.* **1995**, *12*, 99–108. [CrossRef]
12. Alshibli, K.A.; Cil, M.B. Influence of particle morphology on the friction and dilatancy of sand. *J. Geotech. Geoenvironmental Eng.* **2018**, *144*, 04017118. [CrossRef]
13. Lim, M.S.; Wijeyesekera, D.C.; Zainorabidin, A.; Bakar, I. The effects of particle morphology (shape and sizes) characteristics on its engineering behaviour and sustainable engineering performance of sand. *Int. J. Integr. Eng.* **2012**, *4*, 27–37.
14. Abbireddy, C.O.R.; Clayton, C.R.I. The impact of particle form on the packing and shear behaviour of some granular materials: An experimental study. *Granul. Matter* **2015**, *17*, 427–438. [CrossRef]
15. Wadell, H.A. Volume, shape and roundness of rock particles. *J. Geol.* **1932**, *40*, 443–451. [CrossRef]
16. Rittenhouse, G.; Thorp, E.M. Heavy minerals in sediment-transportation studies. *Eos Trans. Am. Geophys. Union* **1943**, *24*, 524. [CrossRef]
17. Powers, M.C. A new roundness scale for sedimentary particles. *J. Sedimentray Res.* **1953**, *23*, 117–119.
18. Krumbein, W.C.; Sloss, L.L. *Stratigraphy and Sedimentation*; W. H. Freeman: New York, NY, USA, 1955.
19. Swanson, P.A.; Vetter, A.F. The Measurement of Abrasive Particle Shape and Its Effect on Wear. *ASLE Trans.* **1985**, *28*, 225–230. [CrossRef]
20. Zheng, J.; Hryciw, R.D. Traditional soil particle sphericity, roundness and surface roughness by computational geometry. *Géotechnique* **2015**, *65*, 494–506. [CrossRef]
21. Mitchell, J.K. Fundamentals of soil behavior. *Soil Sci. Soc. Am. J.* **1976**, *40*, 827–866.
22. Frankel, K.L.; Dolan, J.F. Characterizing arid region alluvial fan surface roughness with airborne laser swath mapping digital topographic data. *J. Geophys. Res. Earth Surf.* **2007**, *112*, F02025. [CrossRef]
23. Ouhbi, N.; Voivret, C.; Perrin, G.; Roux, J.N. 3D particle shape modelling and optimization through proper orthogonal decomposition. *Granul. Matter* **2017**, *19*, 86. [CrossRef]
24. Coop, M.R.; Altuhafi, F.N. Changes to particle characteristics associated with the compression of sands. *Géotechnique* **2011**, *61*, 459–471.
25. Li, Y. Effects of particle shape and size distribution on the shear strength behavior of composite soils. *Bull. Eng. Geol. Environ.* **2013**, *72*, 371–381. [CrossRef]
26. Cresswell, A.; Powrie, W. Triaxial tests on an unbonded locked sand. *Géotechnique* **2004**, *54*, 107–115. [CrossRef]
27. Mair, K.; Frye, K.M.; Marone, C. Influence of grain characteristics on the friction of granular shear zones. *J. Geophys. Res.* **2002**, *107*, ECV 4-1–ECV 4-9. [CrossRef]
28. Feng, Z.K.; Xu, W.J.; Lubbe, R. Three-dimensional morphological characteristics of particles in nature and its application for DEM simulation. *Powder Technol.* **2020**, *364*, 635–646. [CrossRef]
29. Xin, T.; Zhengbo, H.; Changfu, C.; Minghua, Z. 3D DEM-FDM Coupled Analysis of the Behavior of an Isolated Geogrid-Encased Stone Column under Axial Loading. *J. Geotech. Geoenvironmental Eng.* **2021**, *147*, 04021028.
30. Xin, T.; Zhengbo, H.; Ming, C.; Changfu, C. 3D discrete element simulation of a geotextile-encased stone column under uniaxial compression testing. *Comput. Geotech.* **2020**, *126*, 103769.
31. Xin, T.; Zhengbo, H.; Longjian, F.; Minghua, Z. Three-dimensional discrete-continuous coupled numerical simulation of a single stone column in soft soils. *Chin. J. Geotech. Eng.* **2021**, *43*, 347–355.
32. Xin, T.; Zhengbo, H.; Weng, L.; Suhua, Z.; Tenglong, L. Micromechanical Numerical Modelling on Compressive Failure of Recycled Concrete using Discrete Element Method (DEM). *Materials* **2020**, *13*, 4329. [CrossRef]
33. Stahl, M.; Konietzky, H. Discrete element simulation of ballast and gravel under special consideration of grain-shape, grain-size and relative density. *Granul. Matter* **2010**, *13*, 417–428. [CrossRef]
34. Meixiang, G.; Jie, H.; Minghua, Z.H. Three-dimensional DEM analysis of single geogrid-encased stone columns under unconfined compression: A parametric study. *Acta Geotech.* **2017**, *12*, 559–572.
35. Indraratna, B.; Ngo, N.T.; Rujikiatkamjorn, C.; Sloan, S.W. Coupled discrete element–finite difference method for analysing the load-deformation behaviour of a single stone column in soft soil. *Comput. Geotech.* **2015**, *63*, 267–278. [CrossRef]
36. Mengmeng, W.; Zhangqi, X.; Jianfeng, W. Constitutive modelling of idealised granular materials using machine learning method. *J. Rock Mech. Geotech. Eng.* **2023**, *15*, 1038–1051.
37. Ma, Q.; Shu, H.; Xiao, H.; Liu, Y. Analysis of direct shear test of incineration slag reinforced with waste tire strips by discrete element method. *Constr. Build. Mater.* **2023**, *398*, 132534. [CrossRef]
38. Li, M.; Zuo, J.; Hu, D.; Shao, J.; Liu, D. Experimental and numerical investigation of microstructure effect on the mechanical behavior and failure process of brittle rocks. *Comput. Geotech.* **2020**, *125*, 103639. [CrossRef]
39. Wu, K.; Sun, W.; Liu, S.; Zhang, X. Study of shear behavior of granular materials by 3D DEM simulation of the triaxial test in the membrane boundary condition. *Adv. Powder Technol.* **2021**, *32*, 1145–1156. [CrossRef]
40. Indraratna, B.; Ionescu, D.; Christie, H.D. Shear Behavior of Railway Ballast Based on Large-Scale Triaxial Tests. *J. Geotech. Geoenvironmental Eng.* **1998**, *124*, 439–449. [CrossRef]